energies

MDPI

Article

FPGA-Based Real-Time Simulation of Externally Excited Synchronous Machines

Yannick Bergheim [1,*], Fabian Jonczyk [1], René Scheer [2] and Jakob Andert [1]

[1] Chair of Mechatronics in Mobile Propulsion, Faculty of Mechanical Engineering, RWTH Aachen University, Forckenbeckstraße 4, 52074 Aachen, Germany
[2] DENSO Automotive Deutschland GmbH, Freisinger Str. 21-23, 85386 Eching, Germany
* Correspondence: yannick.bergheim@rwth-aachen.de

Abstract

Externally excited synchronous machines (EESMs) are a rare-earth-free solution for traction applications. However, variable field excitation and magnetic coupling increase control complexity. Efficient validation of the resulting control functionalities can be carried out using hardware-in-the-loop (HIL) testing, which requires high-fidelity real-time simulation models. This paper presents a semi-analytical, discrete-time EESM model tailored for HIL applications. Nonlinear magnetic saturation and magnetic coupling are captured using an inverted flux–current characteristic combined with a rotating coordinate transformation, which improves resource utilization. Spatial harmonics are included through a Fourier decomposition of the angle-dependent inverse characteristics. Additionally, different loss mechanisms are considered to accurately represent the physical behavior of the machine. The model is parameterized using finite element analysis (FEA) results from a 100 kW salient-pole EESM. It is implemented on a field-programmable gate array to achieve real-time capability at a simulation frequency of 2.5 MHz. Validation results for the typical operating range show deviations below 0.1 % compared to detailed FEA results, demonstrating accurate real-time simulation of the electromagnetic behavior.

Keywords: externally excited synchronous machine; hardware-in-the-loop; real-time simulation; field-programmable gate array; finite element analysis

Academic Editor: Lorand Szabo

Received: 1 March 2026
Revised: 24 March 2026
Accepted: 25 March 2026
Published: 27 March 2026

1. Introduction

Growing environmental, economic, and geopolitical concerns associated with the use of rare-earth materials have increased interest in externally excited synchronous machines (EESMs) as a rare-earth-free alternative for traction applications. Their superior field-weakening capability and reduced energy losses during cruising operation make them attractive for high-efficiency drive systems. However, variable field excitation and magnetic coupling between the field and stator windings introduce complex control challenges [1–9]. The referenced literature highlights recent efforts in control development for EESMs. However, many of these studies transition directly from simulation to prototype hardware, omitting an intermediate validation step.

Hardware-in-the-loop (HIL) is an established method for testing and validating complex control systems in simulated environments. This methodology connects the electronic control unit to a real-time capable plant simulation, enabling closed-loop testing of control functionalities and system interactions without the need for physical prototypes. When applied in early development stages, HIL testing can significantly accelerate development

https://doi.org/10.3390/en19071661

cycles while minimizing experimental risks and costs. Additionally, HIL provides a safe and flexible environment for analyzing system behavior under critical or fault conditions that would be difficult or unsafe to reproduce with real components. However, achieving reliable HIL simulations requires plant models that combine high physical accuracy with real-time capability.

The use of HIL for the development and validation of electric drive systems is well-established, as evidenced by comprehensive literature reviews [10,11]. However, most existing research has focused on permanent magnet synchronous machines (e.g., [12–14]), reflecting their dominance in automotive traction applications. In addition, real-time modeling of induction machines has been widely explored (e.g., [15–17]), owing to their robustness, structural simplicity, and low drag losses, which make them attractive for cost-sensitive applications. Recent research has increasingly focused on real-time modeling of EESMs. Table 1 summarizes representative modeling approaches, categorized by application focus, considered nonlinearities and loss mechanisms, and real-time capability. Existing approaches can be broadly classified into simplified models developed for control design or more detailed plant models intended for high-fidelity simulation.

Table 1. Comparison of modeling approaches for EESM with respect to nonlinearities, loss mechanisms, and real-time capability.

	Nonlinearities				**Loss Mechanisms**				
	Magnetic Saturation	**Magnetic Coupling**	**Spatial Harmonics**	**Winding Temperatures**	**Friction Losses**	**Copper Losses**	**Iron Losses**	**Real-Time Capability**	**References**
Control Optimization						●			[1,2,18]
	●	●				●			[19]
	●	●				●	●		[3]
	●	●			●	●	●		[4]
	●	●						●	[5,20–23]
	●	●				●		●	[6,24]
	●	●		●		●		●	[7,25]
Plant Simulation	●	●	●						[26,27]
	●	●	●				●		[28]
	●	●	●					●	[29]
	●				●	●	●	●	[30]
	●	●	●	●	●	●	●	●	Proposed Model

In control optimization, offline models are primarily used to determine optimal operating points. Simplified models typically assume linear machine behavior, enabling analytical minimization of copper losses [1,2,18]. More advanced offline optimization strategies incorporate magnetic saturation and magnetic coupling through multidimensional lookup tables (LUTs), thus requiring numerical solution methods [19]. Extensions that include iron losses [3,4] and friction losses [4] further improve machine efficiency but increase complexity. Beyond offline optimization, several studies integrate real-time capable nonlinear machine models into controller synthesis. Magnetic saturation and magnetic coupling are often considered to improve dynamic control performance [5,20,21], enable sensorless control [22], and analyze fault scenarios, such as active short circuits [23]. Furthermore, online copper loss minimization accounting for nonlinear magnetic saturation and magnetic coupling is demonstrated in [6,24], and is further extended to include temperature-dependent stator and field winding resistances in [7,25]. However, spatial harmonics and iron losses are usually neglected in control-oriented real-time models due to their complex modeling and high computational cost.

In contrast, plant simulation models tend to incorporate a broader range of nonlinearities and loss mechanisms in order to achieve a higher level of fidelity. An equivalent circuit model is presented in [26], while [27] proposes a semi-analytical formulation. In both cases, the multidimensional LUTs used to represent magnetic saturation and magnetic coupling are extended by an additional dimension to account for spatial harmonics. Another semi-analytical model that incorporates an additional LUT to represent iron losses is introduced in [28]. While these models demonstrate high accuracy when validated against finite element analysis, they do not achieve real-time capability. In [29], a semi-analytical model based on multidimensional inductance matrices is proposed to capture magnetic saturation, magnetic coupling, and spatial harmonics. Although loss mechanisms are not considered, the model achieves real-time capability through implementation on a field-programmable gate array (FPGA). In contrast, [30] uses simplified analytical formulations for magnetic saturation, friction, copper losses, and iron losses to ensure real-time capability.

The literature review reveals that only a limited number of approaches combine detailed physical modeling with real-time capability, highlighting the trade-off between model fidelity and computational efficiency. To address this gap, this paper proposes a comprehensive plant model that can serve as a virtual prototype for reliable HIL simulations. Section 2 presents an analytical description of EESMs and outlines the modeling of the relevant loss mechanisms. Section 3 describes an FEA-based parameter identification of a 100 kW EESM, which is used to parameterize the semi-analytical discrete-time model derived in Section 4. In Section 5, the model is implemented on an FPGA and the resulting real-time simulation is validated against FEA results.

2. Analytical Description

In the analytical model, the three-phase stator winding is assumed to be symmetrically distributed and connected in a wye configuration. The neutral point is considered isolated, and displacement currents are neglected. Consequently, zero-sequence components are omitted in the rotor-oriented (dq) reference frame. The salient-pole rotor is equipped with a field winding that is supplied with direct current via carbon brushes and slip rings. The corresponding dynamic voltage equations are expressed as follows:

$$u_\mathrm{d} = R_\mathrm{s}(\vartheta_\mathrm{s}) \cdot i_\mathrm{d} + \frac{d\psi_\mathrm{d}}{dt} - \omega_\mathrm{el} \cdot \psi_\mathrm{q} \tag{1}$$

$$u_\mathrm{q} = R_\mathrm{s}(\vartheta_\mathrm{s}) \cdot i_\mathrm{q} + \frac{d\psi_\mathrm{q}}{dt} + \omega_\mathrm{el} \cdot \psi_\mathrm{d} \tag{2}$$

$$u_\mathrm{f,term} = \underbrace{R_\mathrm{f}(\vartheta_\mathrm{f}) \cdot i_\mathrm{f} + \frac{d\psi_\mathrm{f}}{dt}}_{u_\mathrm{f}} + \underbrace{u_\mathrm{0,br} + R_\mathrm{br} \cdot i_\mathrm{f}}_{u_\mathrm{br}} \tag{3}$$

The stator equations involve the voltages u_d and u_q, the currents i_d and i_q, the magnetic flux linkages ψ_d and ψ_q, the stator winding resistance R_s, and the electrical angular velocity ω_el. The subscripts d and q denote the direct and quadrature axes of the rotating reference frame aligned with the rotor field. For the field winding, the model includes the terminal voltage $u_\mathrm{f,term}$, the current i_f, the flux linkage ψ_f, and the winding resistance

R_f. Furthermore, the voltage drop across the brush contacts u_br is described by a constant contact voltage component $u_\mathrm{0,br}$ and a current-dependent term involving the brush contact resistance R_br [4]. Both winding resistances R_s and R_f are modeled with a linear temperature dependence, assuming homogeneous stator and field winding temperatures ϑ_s and ϑ_f. The electromagnetic system equations can be represented by the equivalent dynamic circuit shown in Figure 1.

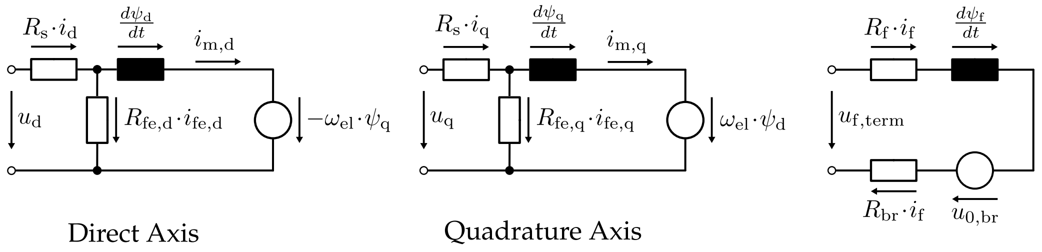

(a) Stator (b) Rotor

Figure 1. Equivalent dynamic circuit of an EESM in rotor-fixed (dq) reference frame including parallel iron loss resistances $R_\mathrm{fe,d}$ and $R_\mathrm{fe,q}$ based on [31,32].

For a comprehensive model, the different loss mechanisms associated with the energy conversion process need to be considered. The total losses are primarily composed of friction losses, copper losses, and iron losses.

Friction losses P_fric represent mechanical losses caused by bearing friction, brush friction and windage, and are analytically approximated following the approach presented in [4].

$$P_\mathrm{fric} = c_\mathrm{brg} \cdot \frac{n_\mathrm{mech}}{n_\mathrm{mech,N}} + c_\mathrm{air} \cdot \left(\frac{n_\mathrm{mech}}{n_\mathrm{mech,N}} \right)^3 \tag{4}$$

The first term represents the linear speed-dependent losses due to bearing and brush friction, combined into the constant friction coefficient c_brg. The second term, scaled with c_air, accounts for windage losses and reflects their cubic dependence on speed. The mechanical speed n_mech is normalized with respect to the rated speed $n_\mathrm{mech,N}$. The coefficients c_brg and c_air can be estimated analytically from the machine geometry and physical properties, or identified experimentally from mechanical loss measurements such as coast-down or drag torque tests.

Copper losses P_cu consist of conduction losses in the stator and rotor windings, as well as electrical losses at the brush contacts. Conduction losses are represented by the ohmic voltage drops across the temperature-dependent winding resistances $R_\mathrm{s}(\vartheta_\mathrm{s})$ and $R_\mathrm{f}(\vartheta_\mathrm{f})$. Electrical losses at the brush contacts originate from the contact resistance between the brushes and slip rings and are accounted for in the voltage drop u_br.

Iron losses P_fe in the soft magnetic cores of the stator and rotor are considered as the sum of hysteresis and eddy current losses. These losses can be modeled using parallel iron loss resistances $R_\mathrm{fe,d}$ and $R_\mathrm{fe,q}$ based on [31,32]. The associated iron loss currents $i_\mathrm{fe,d}$ and $i_\mathrm{fe,q}$ reduce the magnetization currents $i_\mathrm{m,d}$ and $i_\mathrm{m,q}$, thereby affecting the resulting torque. The following steady-state energy balance shows that iron losses can be incorporated directly by using a torque equivalent.

$$\begin{aligned}
T_\mathrm{mech} &= p \cdot (\psi_\mathrm{d} \cdot i_\mathrm{m,q} - \psi_\mathrm{q} \cdot i_\mathrm{m,d}) - \frac{P_\mathrm{fric}}{\omega_\mathrm{mech}} \\
T_\mathrm{mech} &= p \cdot (\psi_\mathrm{d} \cdot i_\mathrm{q} - \psi_\mathrm{q} \cdot i_\mathrm{d}) - p \cdot (\psi_\mathrm{d} \cdot i_\mathrm{fe,q} - \psi_\mathrm{q} \cdot i_\mathrm{fe,d}) - \frac{P_\mathrm{fric}}{\omega_\mathrm{mech}} \\
T_\mathrm{mech} &= p \cdot (\psi_\mathrm{d} \cdot i_\mathrm{q} - \psi_\mathrm{q} \cdot i_\mathrm{d}) - \frac{p}{\omega_\mathrm{el}} \cdot \left(R_\mathrm{fe,q} \cdot {i_\mathrm{fe,q}}^2 + R_\mathrm{fe,d} \cdot {i_\mathrm{fe,d}}^2 \right) - \frac{P_\mathrm{fric}}{\omega_\mathrm{mech}} \\
T_\mathrm{mech} &= p \cdot (\psi_\mathrm{d} \cdot i_\mathrm{q} - \psi_\mathrm{q} \cdot i_\mathrm{d}) - \frac{P_\mathrm{fe}}{\omega_\mathrm{mech}} - \frac{P_\mathrm{fric}}{\omega_\mathrm{mech}}
\end{aligned}$$

Here, ω_{mech} denotes the mechanical angular velocity, with $\omega_{\mathrm{el}} = p \cdot \omega_{\mathrm{mech}}$. With this approach, iron losses during dynamic operation are evaluated based on the instantaneous magnetic operating point, assuming quasi-instantaneous magnetization of the material. This implies quasi-stationary magnetic conditions and neglects dynamic hysteresis and magnetic history effects. Nevertheless, it captures the operating-point-dependent average iron losses commonly described by classical loss-separation models [33].

Consequently, to obtain the mechanical torque T_{mech} at the shaft of the electric machine, the torque equivalents of the iron losses T_{fe} and friction losses T_{fric} are subtracted from the electromagnetic torque T_{em}.

$$T_{\mathrm{mech}} = T_{\mathrm{em}} - T_{\mathrm{fe}} - T_{\mathrm{fric}} \tag{5}$$

3. Parameter Identification

Magnetic saturation, magnetic coupling, and spatial harmonics introduce significant nonlinearities into the operating behavior of EESMs. Consequently, the flux linkage components ψ_{d}, ψ_{q}, and ψ_{f} are modeled as nonlinear functions of the currents i_{d}, i_{q}, and i_{f}, as well as the electrical angle φ_{el}.

$$\psi_{\mathrm{d}} = f_{\psi_{\mathrm{d}}}(i_{\mathrm{d}}, i_{\mathrm{q}}, i_{\mathrm{f}}, \varphi_{\mathrm{el}}) \tag{6}$$

$$\psi_{\mathrm{q}} = f_{\psi_{\mathrm{q}}}(i_{\mathrm{d}}, i_{\mathrm{q}}, i_{\mathrm{f}}, \varphi_{\mathrm{el}}) \tag{7}$$

$$\psi_{\mathrm{f}} = f_{\psi_{\mathrm{f}}}(i_{\mathrm{d}}, i_{\mathrm{q}}, i_{\mathrm{f}}, \varphi_{\mathrm{el}}) \tag{8}$$

Furthermore, the different loss mechanisms depend on the operating point. While friction and copper losses can be described analytically with reasonable accuracy, iron losses exhibit a multidimensional dependence on operating conditions. Therefore, iron losses P_{fe} are modeled as nonlinear functions of the currents i_{d}, i_{q}, and i_{f}, and the mechanical speed n_{mech}.

$$P_{\mathrm{fe}} = f_{P_{\mathrm{fe}}}(i_{\mathrm{d}}, i_{\mathrm{q}}, i_{\mathrm{f}}, n_{\mathrm{mech}}) \tag{9}$$

Accurate modeling of EESMs therefore requires a detailed characterization of their operating behavior. For a physical prototype, this characterization can be performed using a high-voltage traction test bench. Within a model-based development approach, the electromagnetic behavior is analyzed using the finite element method (FEM), a numerical technique for evaluating electromagnetic fields and magnetic flux distributions in the complex geometries of electric machines.

In this work, the salient-pole EESM specified in Table 2 is characterized using the commercial FEM software JMAG-Designer. To balance accuracy and computational cost, a two-dimensional (2D) finite element model is used instead of a detailed three-dimensional (3D) one. As demonstrated in [14], 2D modeling is sufficient for most test scenarios, particularly in the absence of rotor skewing. To further reduce computational effort, anti-periodic symmetry is exploited, limiting the model to a sector of $\frac{360^\circ}{2 \cdot p}$. The resulting 2D model of the active parts is shown alongside Table 2.

The parameter identification is performed using a current-driven magnetic field transient analysis. Sinusoidal phase currents and constant field currents are applied to the stator and rotor windings, respectively, with an operating point distribution of $\Delta i_{\mathrm{d}} = \Delta i_{\mathrm{q}} = 50\,\mathrm{A}$ and $\Delta i_{\mathrm{f}} = 2\,\mathrm{A}$. With the maximum stator and field currents specified in Table 2, this results in a cartesian grid with 1656 operating points. Each simulation case requires approximately 80 s to solve on a standard workstation equipped with an AMD Ryzen 9 5900X CPU, employing a single-core license and a direct solver.

Table 2. Specifications and geometry of the finite element model.

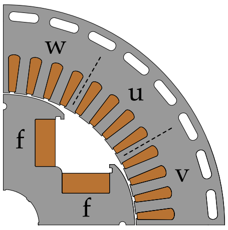

Description	Symbol	Value	Unit
DC-link voltage	u_{dc}	400	V
Max. rotational speed	$n_{\mathrm{mech,max}}$	11,000	min^{-1}
Max. torque	$T_{\mathrm{mech,max}}$	255	N m
Max. power	$P_{\mathrm{mech,max}}$	100	kW
Max. stator current	$i_{\mathrm{s,max}}$	300	$\mathrm{A_{rms}}$
Max. field current	$i_{\mathrm{f,max}}$	10	A
Axial active length	l_{active}	173.5	mm
Stator outer diameter	d_{stator}	260.0	mm

The results of the finite element analysis (FEA) are presented below. For clarity, quantities in the dq-reference frame are averaged over one electrical period, thereby eliminating zero-mean effects such as spatial harmonics. Since the rotor is mirror-symmetric with respect to the d-axis, the magnetic state remains unchanged when ψ_{d} is constant and ψ_{q} is inverted, resulting in mirror-symmetric electromagnetic behavior in the dq-plane [32]. Consequently, the following figures are limited to positive values of i_{q}. It should be noted that the plotted quantities are given in the power-invariant unit system.

Figure 2 presents the flux linkages ψ_{d}, ψ_{q}, and ψ_{f} in the dq-plane for different field currents i_{f}. The flux linkage ψ_{d} clearly reflects the saturation behavior of the soft magnetic core material, as the incremental gain of flux with respect to current decreases with increasing current i_{d}, resulting in wider spacing between adjacent isolines. In addition, the curvature of the ψ_{d} and ψ_{q} isolines indicates pronounced magnetic cross-coupling, showing that the flux linkage in each axis is not solely determined by its corresponding current, but is also affected by the current component of the perpendicular axis. With increasing field cur-

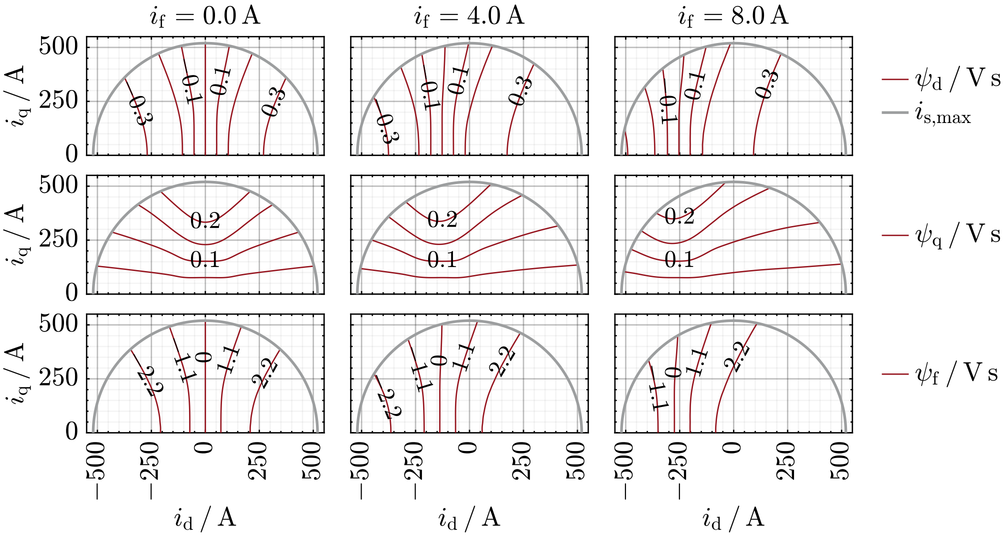

Figure 2. Flux linkages ψ_{d}, ψ_{q}, and ψ_{f} obtained from finite element analysis, represented in the dq-plane for different field currents i_{f}.

rent i_f, the field magnetization shifts the ψ_d isolines towards the negative d-axis direction, reflecting the direct magnetic coupling of f- and d-axis. Due to magnetic cross-coupling, a corresponding shift is also observed in the ψ_q isolines.

The derived electromagnetic torque T_em is shown for different field currents i_f in Figure 3. With zero field current, the torque isolines exhibit the characteristic behavior of a reluctance machine, with torque proportional to the product $i_\text{d} \cdot i_\text{q}$. This behavior results from the saliency-induced torque component, which dominates in the absence of field excitation. As the field current i_f increases, the isolines shift towards the negative d-axis direction. Consequently, the maximum achievable torque increases, reflecting the strengthening influence of the field excitation on the overall magnetic field.

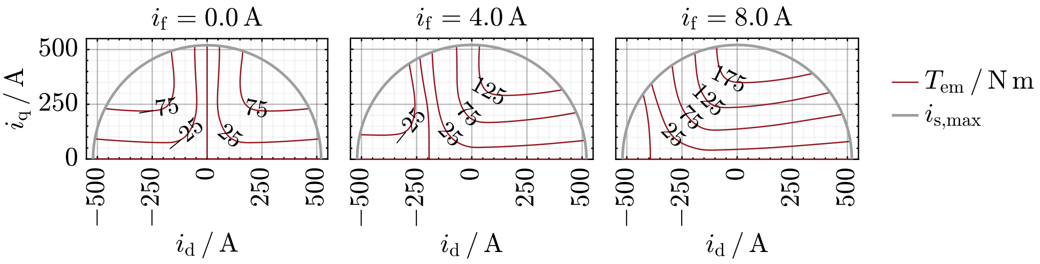

Figure 3. Electromagnetic torque T_em obtained from finite element analysis, represented in the dq-plane for different field currents i_f.

In addition to the magnetic field transient analysis, an iron loss analysis is conducted based on the magnetic flux density distributions to determine the iron losses. Hysteresis losses are calculated using the "Apply Loop Method" [34], and eddy current losses are determined using the "Frequency Analysis Method" [34], both implemented in the FEM software JMAG. Since iron losses depend on both the magnetic flux density and the magnetization frequency, manufacturers provide material-specific iron loss densities as functions of these parameters. To separate hysteresis and eddy current contributions from the total iron loss density, the "Frequency Separation Method" [34] is applied in JMAG. This method relies on the frequency dependence described by Jordan [35], where hysteresis losses scale linearly with frequency and eddy current losses scale quadratically.

Figure 4 illustrates the iron losses P_fe in the dq-plane for different field currents i_f at a fixed mechanical speed of $n_\text{mech} = 1000\,\text{min}^{-1}$. Due to their dependence on the magnetic flux density, the iron losses reflect the elliptical shape of stator flux linkage isolines, including the shift towards negative d-axis direction with increasing field current. The dependence of the iron losses on the mechanical speed is discussed in Section 4.4.

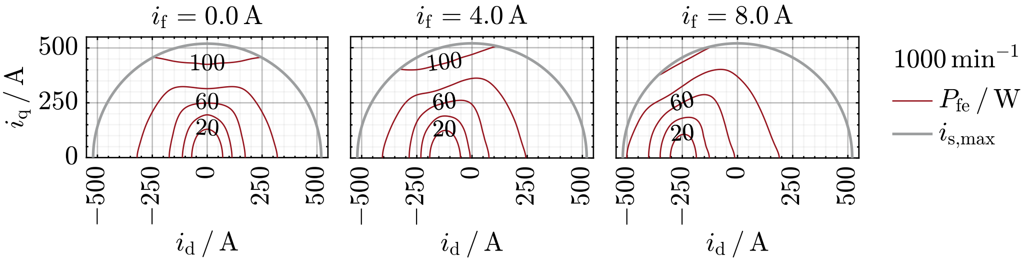

Figure 4. Iron losses P_fe obtained from finite element analysis at $n_\text{mech} = 1000\,\text{min}^{-1}$, represented in the dq-plane for different field currents i_f.

The presented finite element model captures the functional dependencies of flux linkage, electromagnetic torque, and iron losses on the current components i_d, i_q, and i_f. In addition, it incorporates the dependence of flux linkage and torque on the electrical angle φ_el, as well as the dependence of iron losses on the mechanical speed n_mech. Based on these

FEM results, the parameterization of the semi-analytical discrete-time model introduced in the next chapter is derived.

4. Discrete-Time Modeling

Based on the analytical description and identified operating characteristics, a discrete-time simulation model for EESMs is developed with a focus on real-time execution on FPGAs. The objective is to closely approximate the continuous-time behavior using a semi-analytical modeling approach that incorporates nonlinearities and loss mechanisms. The signal flow diagram of the proposed simulation model is shown Figure 5, with the highlighted elements defining the structure of Section 4.

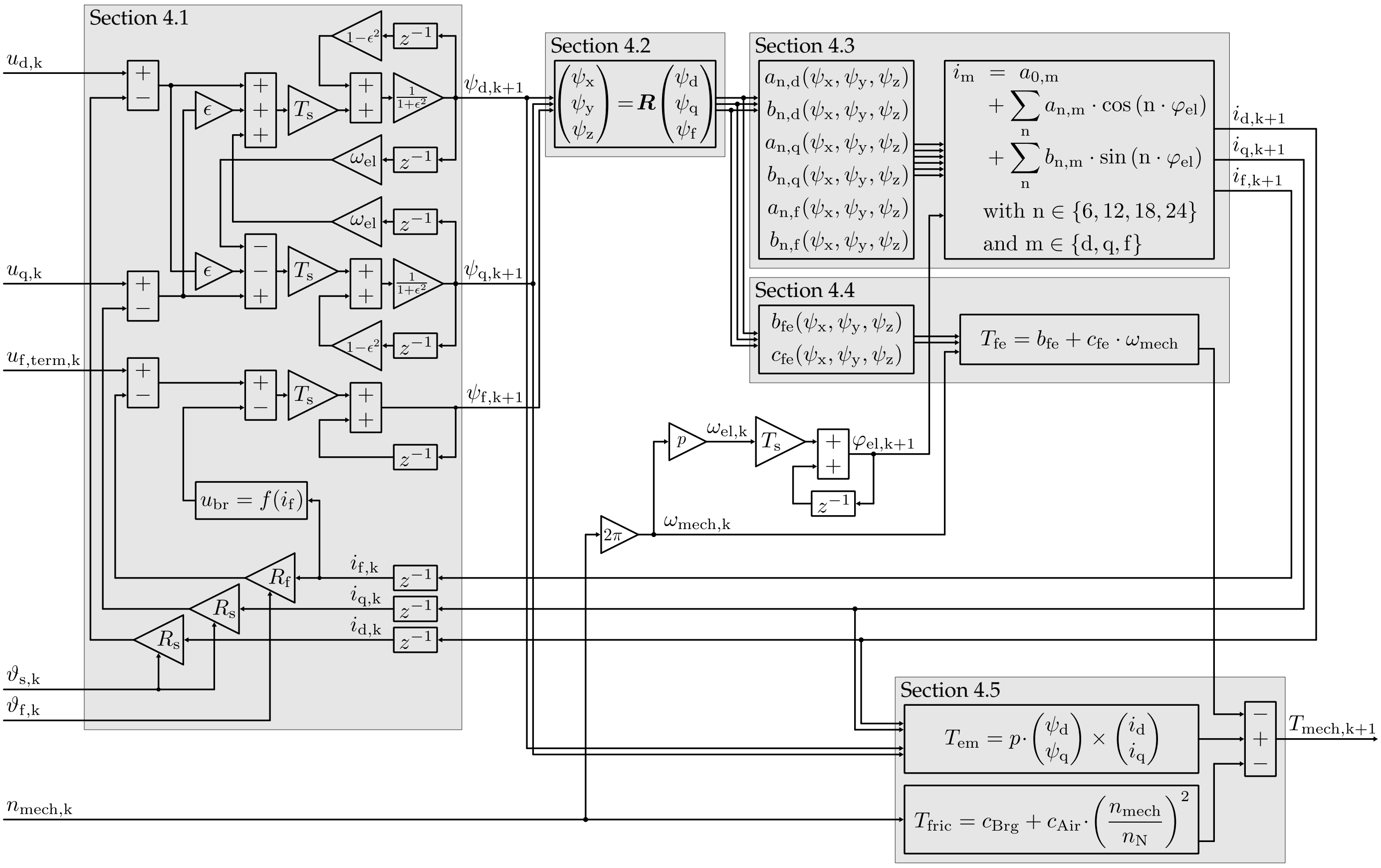

Figure 5. Signal flow diagram of the proposed discrete-time simulation model.

In Section 4.1, the flux linkage-based system equations are discretized using an explicit numerical integration scheme. Nonlinearities caused by magnetic saturation, magnetic coupling, and spatial harmonics are captured by inverting the flux–current characteristic. Thus, the invertibility of this characteristic is analyzed in Section 4.2 to motivate an improved coordinate system. A rotating coordinate transformation is introduced to optimize the grid point distribution, thereby reducing memory requirements and improving interpolation accuracy. This approach is extended in Section 4.3 to incorporate spatial harmonic effects through a Fourier-based reconstruction of the angle-dependent inverse flux–current characteristic, capturing the dominant harmonic orders. Additionally, the different loss mechanisms are considered. Copper losses are included directly in the system equations, with temperature-dependent winding resistances reflecting the dominant thermal influence. Iron losses are modeled in Section 4.4 using flux-linkage-dependent coefficients and a quadratic dependence on mechanical speed. Mechanical losses are modeled as speed-dependent effects in Section 4.5.

4.1. Discretization of Electromagnetic System Equations

The dynamic behavior of EESMs is described using the voltage equations in the rotor-fixed coordinate system. These equations involve the time derivatives of the flux linkages and can be rearranged into explicit first-order ordinary differential equations (ODEs).

$$\frac{d\psi_\mathrm{d}}{dt} = u_\mathrm{d} - R_\mathrm{s} \cdot i_\mathrm{d} + \omega_\mathrm{el} \cdot \psi_\mathrm{q} \tag{10}$$

$$\frac{d\psi_\mathrm{q}}{dt} = u_\mathrm{q} - R_\mathrm{s} \cdot i_\mathrm{q} - \omega_\mathrm{el} \cdot \psi_\mathrm{d} \tag{11}$$

$$\frac{d\psi_\mathrm{f}}{dt} = u_\mathrm{f,term} - R_\mathrm{f} \cdot i_\mathrm{f} - (u_\mathrm{0,br} + R_\mathrm{br} \cdot i_\mathrm{f}) \tag{12}$$

Here, the flux linkages serve as state variables, while the resistances are temperature-dependent parameters. The applied voltages and the electrical angular velocity act as system inputs. The currents are algebraic variables given as nonlinear functions of the flux linkages and the electrical rotation angle, resulting in a system of nonlinear ODEs.

For simulation on a digital platform, the continuous-time system is discretized over a fixed sampling interval T_s using numerical integration. There are different numerical integration methods that can be employed to solve differential equations [36]. However, in real-time applications, the integration scheme must balance numerical stability with computational efficiency. Therefore, the trapezoidal rule is commonly used for the simulation of electrical systems [37,38]. This method approximates the integral over each time step T_s by averaging the derivatives at the start and end of the interval [39].

$$\psi_\mathrm{k+1} \approx \psi_\mathrm{k} + \frac{T_\mathrm{s}}{2} \cdot \Big(f(u_\mathrm{k}, \psi_\mathrm{k}) + f(u_\mathrm{k+1}, \psi_\mathrm{k+1}) \Big) \tag{13}$$

As trapezoidal integration is implicit, it normally requires iterative or predictive solution techniques, which can be computationally expensive. For efficient real-time simulation, the trapezoidal integration of the voltage equations can be simplified by assuming that input voltages, currents, resistances, and the electrical angular velocity remain constant within a single integration step.

$$u_\mathrm{k+1} \approx u_\mathrm{k} \quad , \quad i_\mathrm{k+1} \approx i_\mathrm{k} \quad , \quad R_\mathrm{k+1} \approx R_\mathrm{k} \quad , \quad \omega_\mathrm{el,k+1} \approx \omega_\mathrm{el,k}$$

In electrical circuits with modulated voltages, the assumption of constant voltages u is valid for most time intervals but is violated during switching events, where abrupt voltage changes occur. These discontinuities introduce errors in the affected time step and may cause numerical oscillations [38,40]. The magnitude of the errors and the severity of the oscillations depend on the ratio between the switching frequency and the simulation step size. In contrast, the assumption of constant currents i remains robust for larger step sizes, as inductive windings inherently smooth the current response and maintain continuity under switched excitation. However, the accuracy of this assumption decreases with decreasing inductance and increasing step size, particularly at high switching frequencies where rapid current variations occur. The resistances R and the electrical angular velocity ω_el can be treated as constant over a single step, since thermal and mechanical dynamics evolve on slower timescales than the electrical dynamics. If the time step T_s is sufficiently smaller than the dominant electrical time constants of the system, the resulting discretization error remains negligible. Consequently, the simplified trapezoidal integration can be formulated for each flux linkage.

$$\psi_{\mathrm{d,k+1}} \approx \psi_{\mathrm{d,k}} + T_{\mathrm{s}} \cdot \Big(u_{\mathrm{d,k}} - R_{\mathrm{s,k}} \cdot i_{\mathrm{d,k}} + \frac{1}{2} \cdot \omega_{\mathrm{el,k}} \cdot (\psi_{\mathrm{q,k}} + \psi_{\mathrm{q,k+1}}) \Big) \tag{14}$$

$$\psi_{\mathrm{q,k+1}} \approx \psi_{\mathrm{q,k}} + T_{\mathrm{s}} \cdot \Big(u_{\mathrm{q,k}} - R_{\mathrm{s,k}} \cdot i_{\mathrm{q,k}} - \frac{1}{2} \cdot \omega_{\mathrm{el,k}} \cdot (\psi_{\mathrm{d,k}} + \psi_{\mathrm{d,k+1}}) \Big) \tag{15}$$

$$\psi_{\mathrm{f,k+1}} \approx \psi_{\mathrm{f,k}} + T_{\mathrm{s}} \cdot \Big(u_{\mathrm{f,term,k}} - R_{\mathrm{f,k}} \cdot i_{\mathrm{f,k}} - (u_{\mathrm{0,br}} + R_{\mathrm{br}} \cdot i_{\mathrm{f,k}}) \Big) \tag{16}$$

Although the trapezoidal integration method is fundamentally implicit, the coupled structure of Equations (14) and (15) allows for a linear reformulation.

$$\psi_{\mathrm{d,k+1}} \approx \frac{1}{1+\epsilon^2} \cdot \bigg(\psi_{\mathrm{d,k}} \cdot (1-\epsilon^2) + T_{\mathrm{s}} \cdot \Big(u_{\mathrm{d,k}} - R_{\mathrm{s,k}} \cdot i_{\mathrm{d,k}} + \omega_{\mathrm{el,k}} \cdot \psi_{\mathrm{q,k}} + \epsilon \cdot (u_{\mathrm{q,k}} - R_{\mathrm{s,k}} \cdot i_{\mathrm{q,k}}) \Big) \bigg) \tag{17}$$

$$\psi_{\mathrm{q,k+1}} \approx \frac{1}{1+\epsilon^2} \cdot \bigg(\psi_{\mathrm{q,k}} \cdot (1-\epsilon^2) + T_{\mathrm{s}} \cdot \Big(u_{\mathrm{q,k}} - R_{\mathrm{s,k}} \cdot i_{\mathrm{q,k}} - \omega_{\mathrm{el,k}} \cdot \psi_{\mathrm{d,k}} - \epsilon \cdot (u_{\mathrm{d,k}} - R_{\mathrm{s,k}} \cdot i_{\mathrm{d,k}}) \Big) \bigg) \tag{18}$$

$$\psi_{\mathrm{f,k+1}} \approx \psi_{\mathrm{f,k}} + T_{\mathrm{s}} \cdot \Big(u_{\mathrm{f,term,k}} - R_{\mathrm{f,k}} \cdot i_{\mathrm{f,k}} - (u_{\mathrm{0,br}} + R_{\mathrm{br}} \cdot i_{\mathrm{f,k}}) \Big) \tag{19}$$

with $\epsilon = \frac{1}{2} \cdot \omega_{\mathrm{el,k}} \cdot T_{\mathrm{s}}$

This reformulation yields an explicitly solvable trapezoidal integration, eliminating the need for iterative solution steps. Accordingly, the flux linkages at the next time step $t_{\mathrm{k+1}}$ are numerically integrated based on the voltages, currents, resistances and the angular velocity at t_{k}. For sufficiently small step sizes, numerical oscillations caused by input discontinuities are limited, making the method well-suited to efficient real-time simulation on digital platforms.

4.2. Rotating Coordinate Transformation

After integrating the flux linkages $\psi_{\mathrm{k+1}}$, the corresponding currents $i_{\mathrm{k+1}}$ are obtained from the nonlinear flux–current characteristic, which is typically provided in forward form.

$$f_\psi : \underbrace{(i_{\mathrm{d}}, i_{\mathrm{q}}, i_{\mathrm{f}})}_{\boldsymbol{i}_{\mathrm{dqf}}} \mapsto \underbrace{(\psi_{\mathrm{d}}, \psi_{\mathrm{q}}, \psi_{\mathrm{f}})}_{\boldsymbol{\psi}_{\mathrm{dqf}}} \tag{20}$$

Since nonlinearities such as magnetic saturation and magnetic coupling are included in f_ψ, an analytical representation is highly complex. Instead, the function is commonly approximated using multidimensional lookup tables (LUTs) [41]. These tables contain function values for a grid G_i, consisting of equidistant grid vectors $\boldsymbol{i}_{\mathrm{d}}$, $\boldsymbol{i}_{\mathrm{q}}$, and $\boldsymbol{i}_{\mathrm{f}}$.

$$G_i = \boldsymbol{i}_{\mathrm{d}} \times \boldsymbol{i}_{\mathrm{q}} \times \boldsymbol{i}_{\mathrm{f}} \tag{21}$$

To obtain the currents $i_{\mathrm{k+1}}$ from the flux linkages $\psi_{\mathrm{k+1}}$, the function f_ψ must be inverted.

$$f_\psi{}^{-1} : (\psi_{\mathrm{d}}, \psi_{\mathrm{q}}, \psi_{\mathrm{f}}) \mapsto (i_{\mathrm{d}}, i_{\mathrm{q}}, i_{\mathrm{f}}) \tag{22}$$

According to the inverse function theorem, a vector-valued function $f : \mathbb{R}^n \to \mathbb{R}^n$ is locally invertible near a point x_0 if it is continuously differentiable in a neighborhood of x_0 and the determinant of its Jacobian at that point is non-zero. Therefore, f_ψ is invertible only if the following condition is satisfied for every $\boldsymbol{i}_{\mathrm{dqf}}$.

$$\det\left(\frac{\partial f_\psi(\boldsymbol{i}_{\mathrm{dqf}})}{\partial \boldsymbol{i}_{\mathrm{dqf}}} \right) \neq 0 \tag{23}$$

Following [41], the Jacobian is approximated at each grid point in G_i using central finite differences. Then, the sign of the Jacobian determinant is evaluated to address numerical inaccuracies. Since the determinant exhibits a consistent sign over the entire grid, f_ψ is considered invertible.

To compute the inverse function ${f_\psi}^{-1}$, a corresponding grid must be defined based on the flux linkage values. Since the distribution of grid points is crucial to the accuracy of the resulting interpolation, Figure 6 presents a comparison of two different grid configurations.

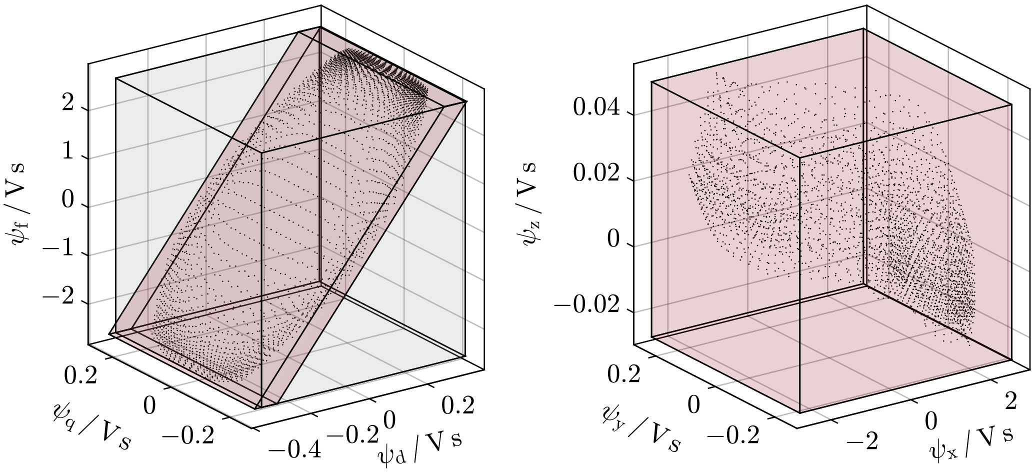

Figure 6. Comparison of a conventional flux linkage grid G_ψ (**left**) and an optimized grid ${G_\psi}^\star$ (**right**), aligned with the direction of direct magnetic coupling.

In both plots, the function values $f_\psi(G_i)$ are depicted as dotted points, highlighting their distribution across the grid. The conventional flux linkage grid G_ψ on the left is constructed from equidistant vectors $\boldsymbol{\psi}_\mathrm{d}$, $\boldsymbol{\psi}_\mathrm{q}$, and $\boldsymbol{\psi}_\mathrm{f}$, covering the full range of flux linkage values encountered in $f_\psi(G_i)$.

$$G_\psi = \boldsymbol{\psi}_\mathrm{d} \times \boldsymbol{\psi}_\mathrm{q} \times \boldsymbol{\psi}_\mathrm{f} \tag{24}$$

However, due to the direct magnetic coupling between the d- and f-axes, the function values concentrate along the diagonal. Consequently, large portions of the conventional grid remain unused, resulting in inefficient memory utilization and increased interpolation errors. To improve accuracy and computational efficiency, an optimized grid ${G_\psi}^\star$ is introduced. It is aligned with the direction of the direct magnetic coupling and more tightly encloses the function values $f_\psi(G_i)$. While [41] determines the orientation of ${G_\psi}^\star$ using principal component analysis, a comparable result is achieved by applying a rotation matrix suited for efficient implementation on digital platforms.

$$\begin{pmatrix} \psi_\mathrm{x} \\ \psi_\mathrm{y} \\ \psi_\mathrm{z} \end{pmatrix} = \boldsymbol{R} \begin{pmatrix} \psi_\mathrm{d} \\ \psi_\mathrm{q} \\ \psi_\mathrm{f} \end{pmatrix} \text{ with } \boldsymbol{R} = \begin{pmatrix} \cos(\gamma) & 0 & \sin(\gamma) \\ 0 & 1 & 0 \\ -\sin(\gamma) & 0 & \cos(\gamma) \end{pmatrix} \tag{25}$$

The rotation matrix $\boldsymbol{R}$ reorients the function values $f_\psi(G_i)$ around the q-axis. The rotation angle γ is selected by minimizing the range of the ψ_z component, resulting in a nearly rectangular distribution of the transformed function values, as depicted in Figure 6 (right). Since the optimal rotation depends on the strength of the magnetic coupling, the rotation angle γ represents a design-specific parameter that is determined offline and kept constant during simulation. Based on the rotated components, the optimized flux linkage grid ${G_\psi}^\star$ is constructed.

$${G_\psi}^\star = \boldsymbol{\psi}_\mathrm{x} \times \boldsymbol{\psi}_\mathrm{y} \times \boldsymbol{\psi}_\mathrm{z} \tag{26}$$

In contrast to the conventional grid G_ψ, which yields fewer than 20 % usable points through inversion of f_ψ, the optimized grid ${G_\psi}^\star$ achieves a utilization of more than 80 %. This substantial improvement demonstrates that aligning the coordinate system with the direction of the direct magnetic coupling reduces memory requirements while achieving high interpolation accuracy.

4.3. Inverse Flux–Current Characteristic

After transforming the integrated flux linkages $\psi_{\mathrm{k+1}}$ into the optimized coordinate system, the corresponding currents $i_{\mathrm{k+1}}$ are obtained from the inverse flux–current characteristic. To account for spatial harmonics, the dependence of the flux–current characteristic on the electrical angle φ_{el} must be included in ${f_\psi}^{-1}$.

$$ {f_\psi}^{-1} : (\underbrace{\psi_{\mathrm{x}}, \psi_{\mathrm{y}}, \psi_{\mathrm{z}}}_{\boldsymbol{\psi}_{\mathrm{xyz}}}, \varphi_{\mathrm{el}}) \mapsto (\underbrace{i_{\mathrm{d}}, i_{\mathrm{q}}, i_{\mathrm{f}}}_{\boldsymbol{i}_{\mathrm{dqf}}}) \tag{27} $$

To evaluate the inverse characteristic at $t_{\mathrm{k+1}}$, the electrical angle φ_{el} is extrapolated assuming constant electrical angular velocity ω_{el} within one integration step.

$$ \varphi_{\mathrm{el,k+1}} \approx \varphi_{\mathrm{el,k}} + T_{\mathrm{s}} \cdot \omega_{\mathrm{el,k}} \tag{28} $$

The inversion is performed sequentially for discrete angular positions, resulting in separate 3D inversions. Each inversion is obtained numerically by solving the following optimization problem.

$$ \min_{\boldsymbol{i}_{\mathrm{dqf}}} \left\| f_\psi(\boldsymbol{i}_{\mathrm{dqf}}) - \boldsymbol{\psi}_{\mathrm{xyz}} \right\|, \qquad \forall\, \boldsymbol{\psi}_{\mathrm{xyz}} \in {G_\psi}^\star \tag{29} $$

The optimization is carried out using the `fsolve` function from MATLAB (R2024b), employing a trust-region dogleg algorithm and a higher-order interpolation of $f_\psi(G_i)$ based on the `makima` scheme. Initializing the solver with the grid point $f_\psi(G_i)$ closest to the desired flux vector $\boldsymbol{\psi}_{\mathrm{xyz}}$ accelerates convergence [41]. The accuracy of the inversion for an individual flux vector $\boldsymbol{\psi}_{\mathrm{xyz}}$ is primarily determined by the interpolation scheme applied to f_ψ and the resolution of the underlying grid G_i.

In general, the solution space of the inverted function ${f_\psi}^{-1}$ is constrained by the range of ${G_\psi}^\star$. Consequently, the bounds of the grid vectors $\boldsymbol{\psi}_{\mathrm{x}}$, $\boldsymbol{\psi}_{\mathrm{y}}$, and $\boldsymbol{\psi}_{\mathrm{z}}$ are selected according to the relevant operating range of the electric machine, including a margin of 20 % beyond the expected nominal conditions. This allows for limited extrapolation outside the operating range. However, the extent of feasible extrapolation is inherently limited, as increasing the covered range reduces the achievable local interpolation accuracy.

The interpolation accuracy of the inverted function ${f_\psi}^{-1}$ between grid points is determined by the resolution of the optimized grid ${G_\psi}^\star$. Since the total number of grid points is typically limited by hardware resources, efficiently distributing the grid vectors $\boldsymbol{\psi}_{\mathrm{x}}$, $\boldsymbol{\psi}_{\mathrm{y}}$, and $\boldsymbol{\psi}_{\mathrm{z}}$ is crucial to maximize resource utilization. A key observation regarding the distribution is the clustering of function values near the upper end of the diagonal in the left plot of Figure 6. This accumulation arises from magnetic saturation, which becomes increasingly pronounced at higher flux linkage levels. The upper plots of Figure 7 illustrate this effect using normalized histograms of the flux linkage components ψ_{x}, ψ_{y}, and ψ_{z}, thereby highlighting the empirical probability distribution of the function values $f_\psi(G_i)$.

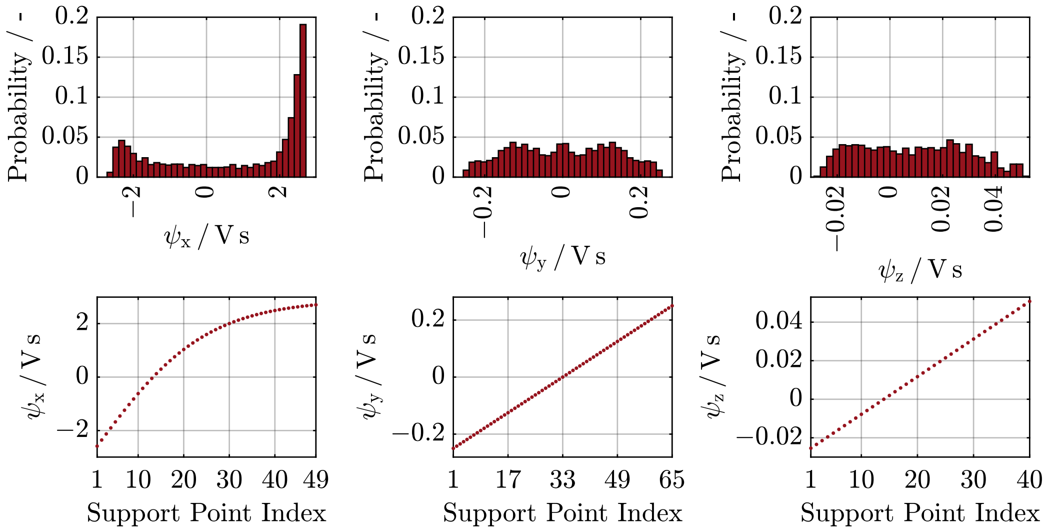

Figure 7. Empirical probability of the functions values $f_\psi(G_i)$ in the optimized grid $G_\psi{}^\star$ (**upper**) and optimized distribution of the grid vectors $\boldsymbol{\psi}_\mathrm{x}$, $\boldsymbol{\psi}_\mathrm{y}$, and $\boldsymbol{\psi}_\mathrm{z}$ to minimize interpolation error (**lower**).

In general, field excitation combined with positive d-axis current results in pronounced magnetic saturation. This leads to a high probability of large ψ_x values due to the grid alignment with the magnetization direction. Conversely, negative ψ_x values occur under low field excitation combined with field weakening caused by negative d-axis current. However, as shown by the electromagnetic torque characteristics in Figure 3, such operating points are of limited practical relevance. To improve interpolation accuracy in the dominant operating region, the vector $\boldsymbol{\psi}_\mathrm{x}$ is defined using a hyperbolic tangent distribution. As a trade-off, larger interpolation errors may occur in less relevant regions with negative ψ_x values. Due to the symmetry of the magnetic state, the flux linkage component ψ_y exhibits a symmetric probability distribution. Moreover, both components ψ_y and ψ_z exhibit an almost uniform distribution. Accordingly, the vectors $\boldsymbol{\psi}_\mathrm{y}$ and $\boldsymbol{\psi}_\mathrm{z}$ are constructed using equidistant spacing. While further machine-specific optimization of the grid point distribution could improve accuracy, the chosen approach provides a robust, generally applicable solution across different machine designs. It should be noted that the total number of grid points in the lower plots of Figure 7 is limited by the hardware resources available on the selected target platform.

After defining the optimized grid $G_\psi{}^\star$, the inversion is performed for each grid point. For a representative flux vector $\boldsymbol{\psi}_\mathrm{xyz}$ from $G_\psi{}^\star$, the left plots of Figure 8 show the resulting current components i_d, i_q, and i_f as functions of the electrical angle φ_el.

The influence of spatial harmonics appears as current ripple components in the inverse characteristics. Due to the magnetomotive force (MMF) distribution of a three-phase winding with 120° phase displacement, spatial harmonics predominantly occur at the sixth order and its multiples [42]. This behavior is confirmed by the discrete Fourier transform (DFT) analysis shown in the right plots of Figure 8. Based on the harmonic content of the inverse current waveforms, their dependence on the electrical angle φ_el can be modeled using Fourier coefficients.

$$i_\mathrm{m} = a_{0,\mathrm{m}} + \sum_\mathrm{n} a_{\mathrm{n},\mathrm{m}} \cdot \cos(\mathrm{n} \cdot \varphi_\mathrm{el}) + \sum_\mathrm{n} b_{\mathrm{n},\mathrm{m}} \cdot \sin(\mathrm{n} \cdot \varphi_\mathrm{el}) \tag{30}$$
$$\text{with } \mathrm{n} \in \{6, 12, 18, 24\} \text{ and } \mathrm{m} \in \{\mathrm{d}, \mathrm{q}, \mathrm{f}\}$$

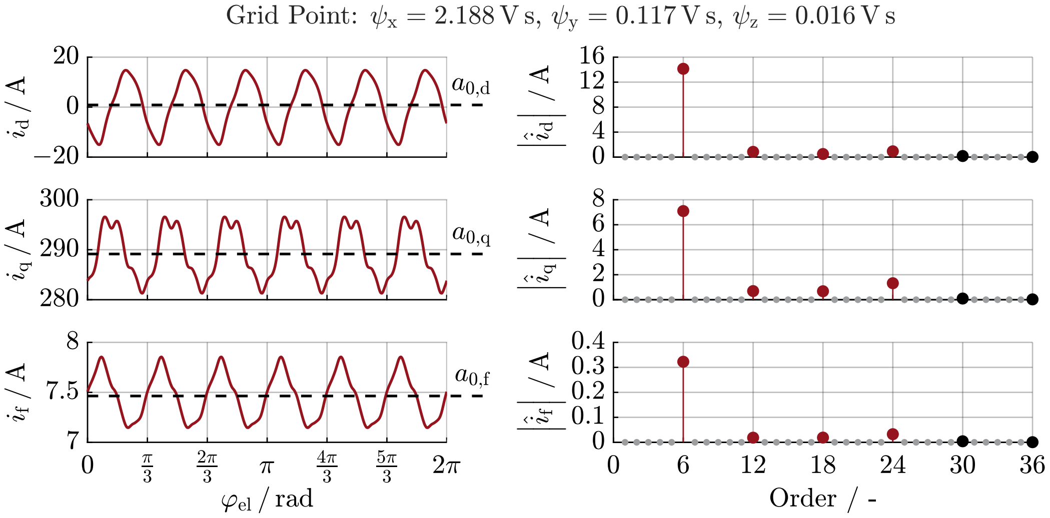

Figure 8. Inverse flux–current characteristic for a flux linkage vector $\boldsymbol{\psi}_{xyz}$ in dependence of the electrical angle φ_{el} (**left**) and a DFT analysis of the harmonic proportions caused by spatial harmonics (**right**).

The coefficients $a_{0,m}$ represent the DC components, while the harmonic coefficients $a_{n,m}$ and $b_{n,m}$ are obtained from the real and imaginary parts of the Fourier spectrum. The reconstruction is confined to the dominant harmonics and truncated at the 24th order, as higher-order contributions are negligible in the FEA results but would increase resource utilization. Consequently, Equation (30) accurately captures the angular variation of the currents while maintaining low computational effort.

Unlike a 4D LUT representation of Equation (27), the Fourier reconstruction provides a compact, accurate model of the angle-dependent waveforms. This approach significantly reduces memory consumption, mitigates interpolation errors, and preserves waveform periodicity. Consequently, the following 27 Fourier coefficients are calculated offline and stored in 3D LUTs to efficiently solve the inverse flux–current characteristic.

$$\begin{aligned} &a_{0,d}(\psi_x,\psi_y,\psi_z), && a_{n,d}(\psi_x,\psi_y,\psi_z), && b_{n,d}(\psi_x,\psi_y,\psi_z), \\ &a_{0,q}(\psi_x,\psi_y,\psi_z), && a_{n,q}(\psi_x,\psi_y,\psi_z), && b_{n,q}(\psi_x,\psi_y,\psi_z), \\ &a_{0,f}(\psi_x,\psi_y,\psi_z), && a_{n,f}(\psi_x,\psi_y,\psi_z), && b_{n,f}(\psi_x,\psi_y,\psi_z), \quad \text{with } n \in \{6,12,18,24\} \end{aligned}$$

Figure 9 shows the DC Fourier coefficients of $f_\psi{}^{-1}(G_\psi{}^\star)$ as functions of ψ_x and ψ_y, evaluated at different levels of ψ_z. Due to the preserved symmetry of the magnetic state in the inversion, all Fourier coefficients are mirror-symmetric about the y-axis. Similar to the flux linkage behavior, a sign inversion must be applied to i_q in the inverse flux–current characteristic. Accordingly, the Fourier coefficients $a_{0,q}$, $a_{n,q}$, and $b_{n,q}$ are scaled by the sign of the flux linkage component ψ_y.

The arrows indicate how the coefficients change with increasing flux linkage ψ_z. Since the x-axis of the optimized coordinate system is aligned with the magnetization direction, variations in the perpendicular z-axis flux linkage are strongly reflected in i_d and i_f. An increase in ψ_z can result from either a decrease in ψ_d or an increase in ψ_f. Consequently, as ψ_z increases, $a_{0,d}$ decreases while $a_{0,f}$ increases. In contrast, $a_{0,q}$ is only indirectly affected through magnetic cross-coupling and therefore exhibits much weaker dependence on ψ_z.

https://doi.org/10.3390/en19071661

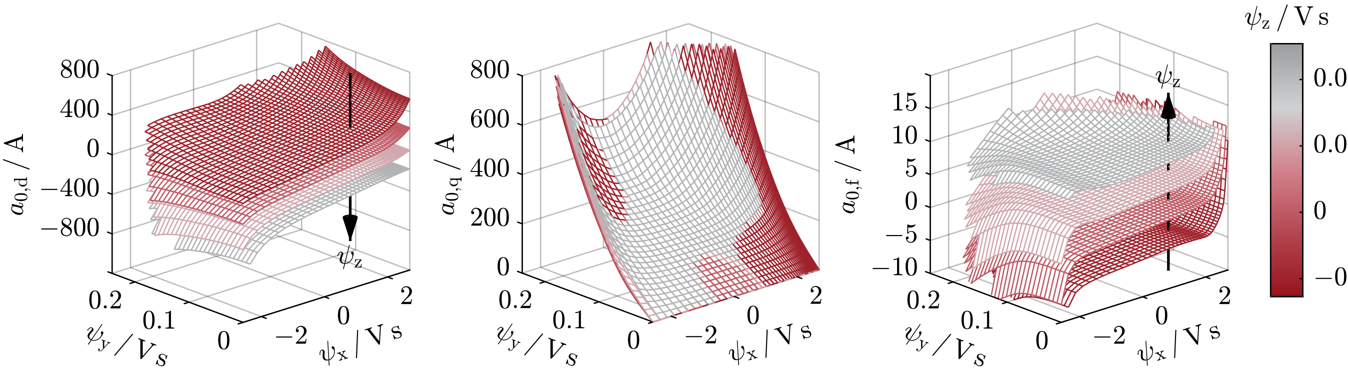

Figure 9. Fourier coefficients $a_{0,\mathrm{d}}$, $a_{0,\mathrm{q}}$, and $a_{0,\mathrm{f}}$ of the inverse flux–current characteristic $f_\psi{}^{-1}(G_\psi{}^\star)$ in dependence of the flux linkages ψ_x, ψ_y, and ψ_z.

The effect of magnetic saturation is most evident in the edge regions of $a_{0,\mathrm{f}}$. Under saturation, a substantial increase in current only results in a minor increase in flux linkage, leading to steep gradients in these areas. While the finer grid resolution accurately captures the curvature of the surfaces for positive values of ψ_x, abrupt gradient changes appear for negative values due to the coarser grid in this region. As a result, larger deviations in the inverted flux–current characteristic are expected for negative values of ψ_x.

To validate the accuracy of the inversion, the absolute deviations are evaluated across the grid G_i. The calculation relies on the mathematical principle, that applying a function followed by its inverse returns the original input.

$$\begin{pmatrix} |\Delta i_\mathrm{d}| \\ |\Delta i_\mathrm{q}| \\ |\Delta i_\mathrm{f}| \end{pmatrix} = \left| f_\psi{}^{-1}\big(f_\psi(\boldsymbol{i}_\mathrm{dqf})\big) - \boldsymbol{i}_\mathrm{dqf} \right|, \qquad \forall\, \boldsymbol{i}_\mathrm{dqf} \in G_i \tag{31}$$

Figure 10 shows the absolute deviations of the inverse flux–current characteristic as functions of i_d and i_q for different levels of i_f. For all three current components, larger deviations occur in the field weakening range, characterized by negative values of i_d. The deviations in i_q are comparatively small due to its weaker dependence on the ψ_z component. Overall, the deviations decrease with increasing field current, since negative ψ_x values then occur only under stronger field weakening conditions. This behavior confirms that the dominant source of the deviations is the coarse grid resolution in regions with negative ψ_x. As a result, higher deviations are confined to operating regions of limited practical relevance, while remaining low within the relevant operating range.

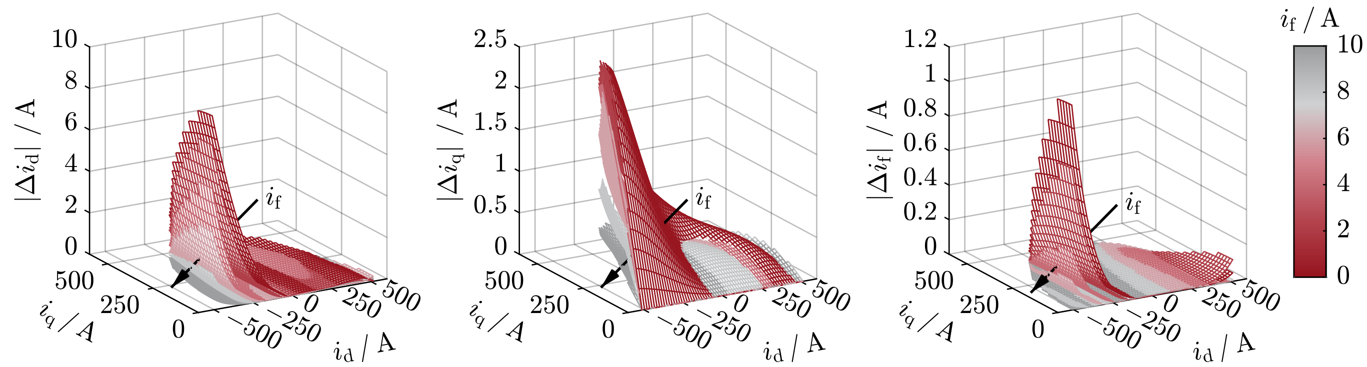

Figure 10. Absolute deviations $|\Delta i_\mathrm{d}|$, $|\Delta i_\mathrm{q}|$, and $|\Delta i_\mathrm{f}|$ of the inverse flux–current characteristic, revealing larger deviations in less relevant regions with negative ψ_x.

https://doi.org/10.3390/en19071661

4.4. Iron Loss Modeling

Figure 11 illustrates the iron losses obtained from FEA for a representative grid point of $G_{\psi}{}^{\star}$ in dependence of the mechanical speed n_{mech}. Following the frequency dependence described by Jordan [35], hysteresis losses exhibit a linear dependence on speed and are described by the coefficient b_{fe}, whereas eddy current losses increase quadratically with speed and are captured by c_{fe}.

$$P_{\text{fe}} = b_{\text{fe}} \cdot \omega_{\text{mech}} + c_{\text{fe}} \cdot \omega_{\text{mech}}{}^{2} \tag{32}$$

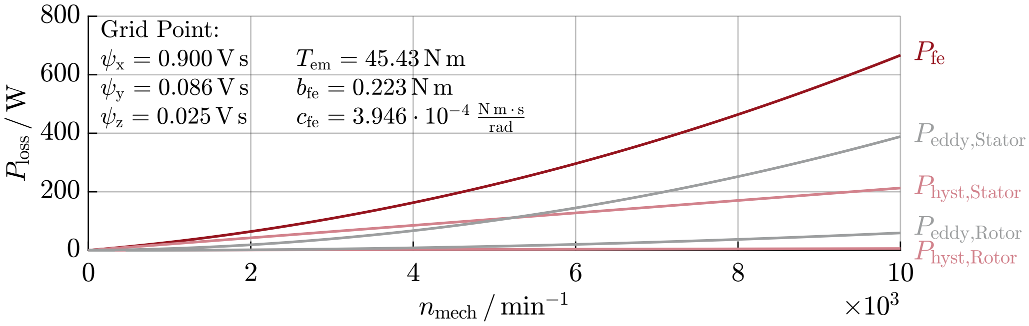

Figure 11. Iron losses P_{fe} for a flux linkage vector $\boldsymbol{\psi}_{\text{xyz}}$ in dependence of the mechanical speed n_{mech}.

The coefficients b_{fe} and c_{fe} are calculated offline and stored in two additional 3D LUTs, enabling an efficient evaluation of the iron losses. Since the flux linkage vector $\boldsymbol{\psi}_{\text{xyz}}$ uniquely describes the magnetic operating point of the EESM, the iron loss coefficients are parameterized as functions of the flux linkages ψ_{x}, ψ_{y}, and ψ_{z}.

$$b_{\text{fe}}(\psi_{\text{x}}, \psi_{\text{y}}, \psi_{\text{z}}), \quad c_{\text{fe}}(\psi_{\text{x}}, \psi_{\text{y}}, \psi_{\text{z}})$$

Once again, the symmetry condition can be exploited to save hardware resources, restricting these LUTs to positive values of ψ_{y}. Since the model primarily captures the overall operating behavior, iron losses are not separated into their components. However, if loss separation is required, the same methodology can be extended.

Figure 12 shows the two iron loss coefficients as functions of the flux linkage components ψ_{x} and ψ_{y} for different levels of ψ_{z}. Both coefficients generally increase with rising flux linkages, reflecting the physical dependence of iron losses on magnetic flux density. With increasing ψ_{z}, the surfaces progressively shift toward positive values of ψ_{x}. Since ψ_{z} is mainly increased by field excitation, negative values of ψ_{x} only occur under stronger field-weakening operation, where the opposing flux contributions of ψ_{d} and ψ_{f} lead to increased iron losses. Conversely, positive ψ_{x} values require a smaller d-axis current contribution, resulting in lower iron losses in these regions.

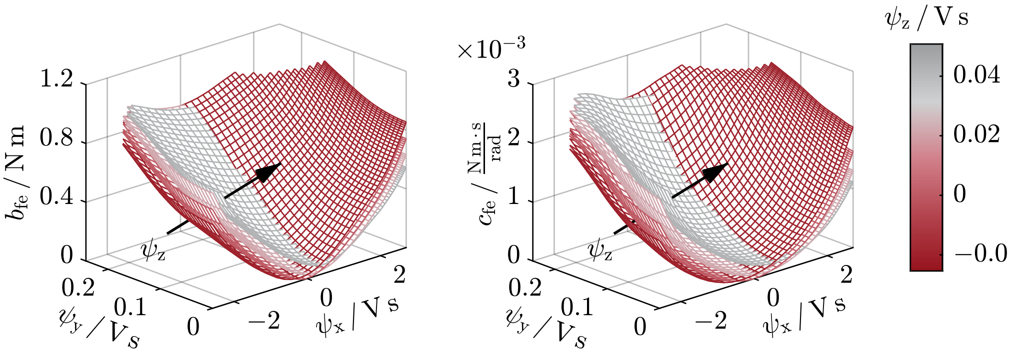

Figure 12. Iron loss coefficients b_{fe} and c_{fe} in dependence of the flux linkages ψ_{x}, ψ_{y}, and ψ_{z}.

4.5. Torque Calculation

In the final computation step, the mechanical torque T_{mech} is evaluated as

$$\begin{aligned} T_{\mathrm{mech,k+1}} = & \underbrace{p \cdot (\psi_{\mathrm{d,k+1}} \cdot i_{\mathrm{q,k+1}} - \psi_{\mathrm{q,k+1}} \cdot i_{\mathrm{d,k+1}})}_{T_{\mathrm{em,k+1}}} \\ & - \underbrace{(b_{\mathrm{fe,k+1}} + c_{\mathrm{fe,k+1}} \cdot \omega_{\mathrm{mech,k}})}_{T_{\mathrm{fe,k+1}}} \\ & - \underbrace{\left(c_{\mathrm{brg}} + c_{\mathrm{air}} \cdot \left(\frac{n_{\mathrm{mech,k}}}{n_{\mathrm{mech,N}}} \right)^2 \right)}_{T_{\mathrm{fric,k+1}}}. \end{aligned} \tag{33}$$

First, the electromagnetic torque T_{em} is computed from the integrated flux linkages $\psi_{\mathrm{k+1}}$ and the corresponding current values $i_{\mathrm{k+1}}$. Then, the torque equivalent of the iron losses T_{fe} is subtracted using the iron loss coefficients $b_{\mathrm{fe,k+1}}$ and $c_{\mathrm{fe,k+1}}$. Finally, the friction torque T_{fric}, based on the constant friction coefficients c_{brg} and c_{air}, is subtracted. The friction coefficients are identified experimentally from mechanical loss measurements of a physical prototype, yielding

$$c_{\mathrm{brg}} = 0.299\,\mathrm{N\,m}, \quad c_{\mathrm{air}} = 0.035\,\mathrm{N\,m}, \quad n_{\mathrm{mech,N}} = 2000\,\mathrm{min}^{-1}.$$

For both loss terms, the mechanical speed n_{mech} is assumed constant within one integration step, due to the relatively slow mechanical dynamics.

5. Real-Time Implementation and Validation

The proposed discrete-time model is integrated into a real-time simulation model of the electric powertrain, which is structured into a plant model and a control model. The plant model comprises the high-fidelity EESM model, complemented by simplified models of the resolver and the power electronics, including a two-level three-phase inverter for the stator and a full-bridge inverter for field winding excitation. All submodels are executed in parallel and synchronized at each simulation step to ensure consistent signal exchange. The control model incorporates an angle-tracking observer and a decoupled field-oriented current control scheme. The gate signals are generated using space vector pulse-width modulation for the two-level inverter and bipolar pulse-width modulation for the full-bridge inverter, both operated at a switching frequency of $f_{\mathrm{s}} = 10\,\mathrm{kHz}$.

The described simulation model is deployed on a real-time simulation platform comprising a dSPACE SCALEXIO Processing Unit and a dSPACE LabBox equipped with a DS6602 FPGA [43]. In order to satisfy the real-time requirements, both the plant and control models are executed on the FPGA. The design is implemented using AMD Vitis Model Composer in combination with the HDL Library for Simulink, which enables automatic VHDL code generation from a block-oriented environment. All signals are implemented using 32-bit fixed-point representations to improve performance and minimize hardware complexity. The binary point is optimized individually for each signal to balance numerical accuracy and dynamic range. The resulting FPGA resource utilization and LUT configuration are summarized in Table 3.

Table 3. FPGA resource utilization and LUT configuration of the proposed real-time model.

Hardware Resource	Used	Utilization
Configurable Logic Blocks	31,250	47.8 %
Configurable Logic Block LUTs	145,810	27.9 %
Configurable Logic Block Flip-Flops	146,761	14.0 %
Block RAM Blocks 36 kB	915	93.0 %
Digital Signal Processor Slices	1304	66.3 %
LUT Configuration		
Number of 3D LUTs	29	
Grid Size per LUT	49 × 33 × 40	

The implementation is primarily dominated by the memory requirements of the 3D LUTs, which account for a significant portion of the utilized block random-access memory (RAM) resources (93 %). A direct implementation of the spatial harmonics using 4D LUTs for Equation (27) would lead to a prohibitive increase in memory requirements due to the exponential growth of the data size. Consequently, such an approach would require either a significant reduction in the existing grid resolution (49 × 33 × 40) or a coarse discretization of the additional dimension, both of which would result in increased interpolation errors.

The EESM model is executed on the FPGA with a sample time of 50 clock cycles. Given an internal clock period of 8 ns, this corresponds to a simulation frequency of 2.5 MHz. Consequently, the FPGA-based plant model operates at a significantly higher rate than the inverter switching frequency and the associated control loop, a technique commonly referred to as asynchronous oversampling. Owing to the high simulation frequency, additional measures such as interpolation of the gate signals are not required to compensate for sampling errors [44,45].

The proposed discrete-time model is validated at steady-state operating points by comparing real-time simulation results with a detailed FEA. To enable acquisition of the high-frequency simulation data, an oscilloscope functionality is implemented directly on the FPGA, utilizing the available 4 GB of onboard RAM. The data are captured with 2.5 MHz to match the simulation frequency of the EESM model. The validation has been performed for a wide range of operating points with comparable results. In the following, two representative operating points are discussed.

Figure 13 shows the simulated currents at a constant operating point. The current waveforms reveal oscillations due to the influence of spatial harmonics, with a dominant sixth-order component that is particularly pronounced in the field current. These low-frequency effects are superimposed by high-frequency, time-harmonic ripples arising from the modulated voltage waveforms.

For a quantitative comparison between the FPGA-based simulation and FEA results, the electromagnetic behavior is re-simulated using the measured current waveforms as input for the FEA. Due to the combination of mechanical speed and high sampling frequency, simulating a single electrical period requires 25,001 FEA time steps. To prevent inaccuracies in the magnetic flux density distribution within the air gap, the mesh in this region must be significantly refined. The increase in both mesh elements and time steps leads to a computation time of approximately 5 h for a single electrical period.

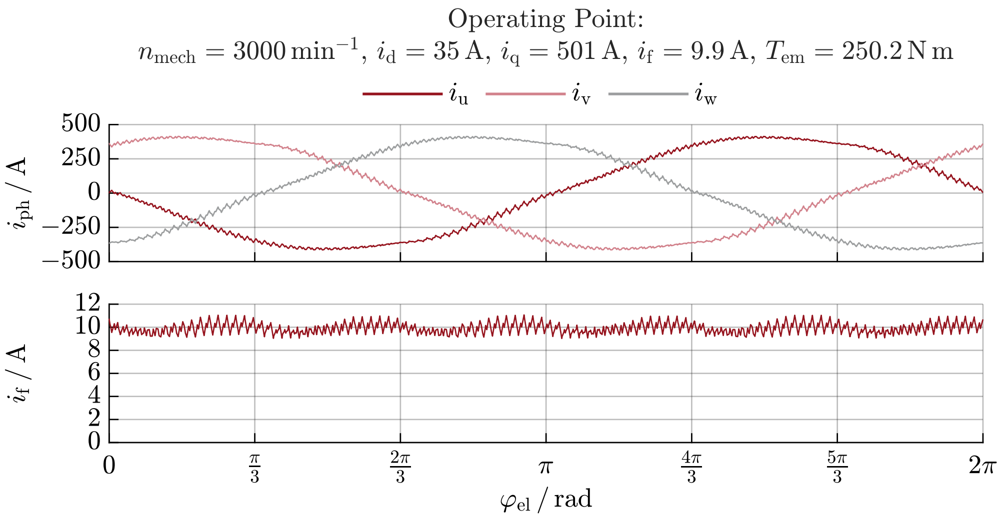

Figure 13. Real-time simulated phase currents i_{u}, i_{v}, i_{w} and field current i_{f}, measured at a constant operating point over one electrical period with a sampling frequency of 2.5 MHz.

Figure 14 presents a validation of the real-time simulation by comparing the resulting flux linkages ψ_{d}, ψ_{q}, and ψ_{f}, as well as the electromagnetic torque T_{em}, against the high-resolution FEA results at a representative operating point within the typical operating range. The results indicate an excellent agreement between the two methods, with relative deviations below 0.1 % for all flux linkages and 0.055 % for the average electromagnetic torque. In addition, the waveform shapes, including space-harmonic and time-harmonic ripple components, are accurately reproduced. Only minor deviations are observed, which are caused by linear interpolation within the LUTs.

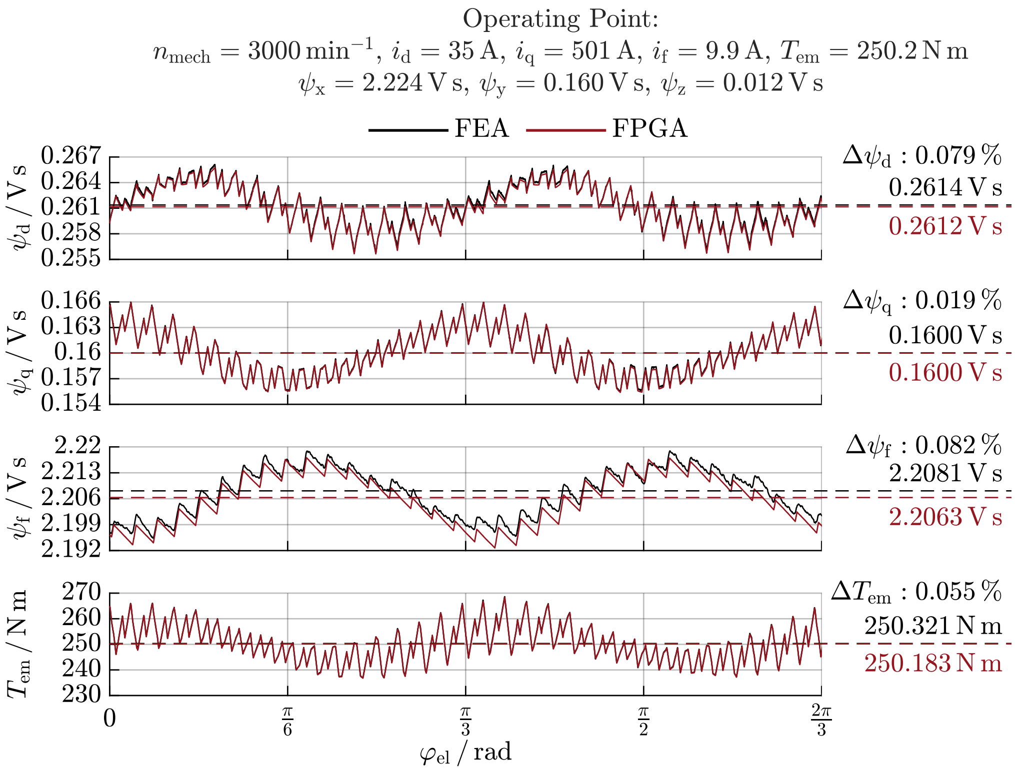

Figure 14. Validation of the real-time simulation against FEA results at a constant operating point representative of the typical operating range. Excellent agreement between FPGA and FEA results with deviations below 0.1 %.

Following the analysis of grid point distribution and the resulting deviations in Section 4.3, an additional validation is presented for an operating point beyond the typical operating range. The operating point shown in Figure 15 is characterized by low field excitation combined with pronounced field weakening, indicated by small values of i_f and large negative values of i_d. Under these conditions, increased deviations in the flux linkage components are observed, ultimately leading to a deviation of approximately 4.5 % in the electromagnetic torque. In comparison to operating points within the typical operating range, the waveform shapes also exhibit noticeably larger discrepancies.

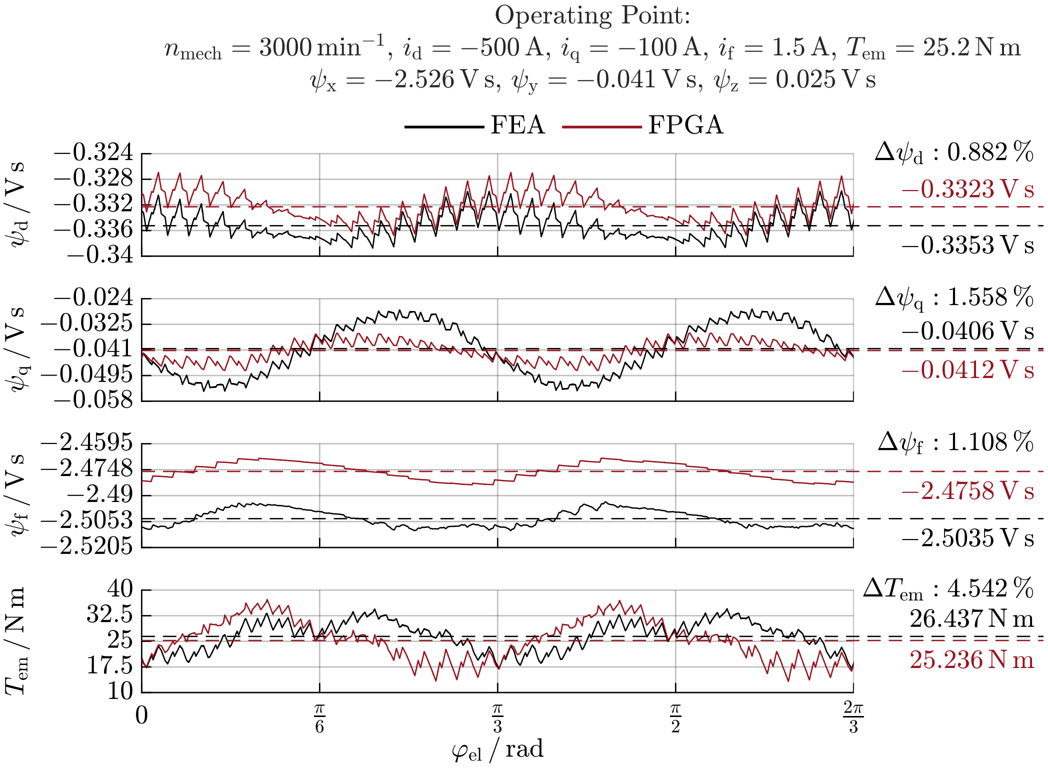

Figure 15. Validation of the real-time simulation against FEA results at a constant operating point beyond the typical operating range, featuring low field excitation and strong field weakening. Deviations between FPGA and FEA results are increased, yet the real-time simulation remains stable.

As expected, deviations increase outside of the typical operating range. If required, the simulation accuracy in these regions can be improved by allocating additional memory. However, since these operating points do not represent standard conditions, the primary requirement is that control overshoots in these extreme regions do not compromise the stability of the simulation. This was verified not only for the presented operating point but also across other conditions, thereby confirming the robustness of the simulation.

6. Conclusions

This paper presents a semi-analytical, discrete-time EESM model tailored for HIL applications. The model incorporates nonlinear magnetic saturation and magnetic coupling using an inverted flux–current characteristic. A rotating coordinate transformation that aligns the coordinate system with the direction of direct magnetic coupling significantly improves memory utilization of the inverted characteristic from 20 % to 80 %. Spatial harmonics are included through a Fourier-based reconstruction of the angular dependency to reduce memory consumption, mitigate interpolation errors, and maintain waveform periodicity. Copper losses are represented by ohmic voltage drops across the temperature-dependent winding resistances and a current-dependent voltage drop across the brush contacts. Friction losses are modeled using an empirical polynomial function of rotational speed, while iron losses are described using operating-point-dependent coefficients stored in three-dimensional LUTs. Implementing the model on an FPGA-based real-time platform demonstrates high accuracy, with deviations of less than 0.1 % compared to FEA within the typical operating range, while maintaining stable simulation behavior beyond it. Consequently, the proposed model is suitable for HIL setups to support robust controller development, calibration, and system-level validation before transitioning to hardware prototypes.

Author Contributions: Conceptualization, Y.B., F.J. and R.S.; methodology, Y.B. and F.J.; software, Y.B. and F.J.; validation, Y.B.; formal analysis, Y.B.; investigation, Y.B.; resources, R.S. and J.A.; data curation, Y.B. and F.J.; writing—original draft preparation, Y.B.; writing—review and editing, F.J., R.S. and J.A.; visualization, Y.B.; supervision, J.A.; project administration, Y.B.; funding acquisition, J.A. All authors have read and agreed to the published version of the manuscript.

Funding: The tests were partially conducted at the Center for Mobile Propulsion (CMP) of the RWTH Aachen University with financial support from the Deutsche Forschungsgemeinschaft (DFG).

Institutional Review Board Statement: Not applicable.

Data Availability Statement: The data from the finite element analysis used for the parameterization of the real-time model are openly available on Zenodo at https://doi.org/10.5281/zenodo.18822007 (accessed on 1 March 2026).

Acknowledgments: The authors would like to thank DENSO Automotive Deutschland GmbH, in particular the Aachen Engineering Center (AEC), for providing access to the test facility within the framework of a collaborative research project.

Conflicts of Interest: Author René Scheer was employed by the company DENSO Automotive Deutschland GmbH. The remaining authors declare that the research was conducted in the absence of any commercial or financial relationships that could be construed as a potential conflict of interest.

Abbreviations

The following abbreviations are used in this manuscript:

ECU	Electronic Control Unit
EESM	Externally Excited Synchronous Machine
FEA	Finite Element Analysis
FEM	Finite Element Method
FPGA	Field-Programmable Gate Array
HIL	Hardware-in-the-Loop
LUT	Lookup Table
ODE	Ordinary Differential Equation
DFT	Discrete Fourier Transform

References

1. Breda, R.; Andrioli, G.; Calligaro, S.; Petrella, R. Extended MTPA and Flux-Weakening Control with Total Copper Loss Minimisation and Transient Torque Compensation for Wound-Rotor Synchronous Machines. In *2023 IEEE Energy Conversion Congress and Exposition (ECCE)*; IEEE: New York, NY, USA, 2023; pp. 4829–4836. [CrossRef]
2. Capitanio, A.; Nuzzo, S.; Sala, G.; Barater, D.; Franceschini, G. Analysis of Externally Excited Synchronous Motors Operation Under Joule Losses Minimization Control. In *2024 International Conference on Electrical Machines (ICEM)*; IEEE: New York, NY, USA, 2024; pp. 1–7. [CrossRef]
3. Carlsson, A.; Andersson, F.; Santantonio, I.; Josefsson, V.; Puccio, G.; Rubino, S. Performance and Efficiency Mapping of Externally Excited Synchronous Machines. In *2024 International Conference on Electrical Machines (ICEM)*; IEEE: New York, NY, USA, 2024; pp. 1–7. [CrossRef]

4. Grune, R. Verlustoptimaler Betrieb Einer Elektrisch Erregten Synchronmaschine für den Einsatz in Elektrofahrzeugen. Ph.D. Dissertation, Technische Universität Berlin, Berlin, Germany, 2013. [CrossRef]
5. Tang, J.; Jiang, B.; Boscaglia, L.; Chen, H.; Liu, Y.; Lundberg, S. Comprehensive Dynamic Current Control of Electrically Excited Synchronous Machines With Magnetic Mutual Couplings. *IEEE Trans. Ind. Electron.* **2024**, *71*, 13855–13866. [CrossRef]
6. Reinhard, J.; Löhe, K.; Graichen, K. Optimal dynamic current control for externally excited synchronous machines. In *2024 IEEE Conference on Control Technology and Applications (CCTA)*; IEEE: New York, NY, USA, 2024; pp. 146–152. [CrossRef]
7. Tang, J.; Jiang, B.; Chen, H.; Liu, Y.; Lundberg, S. Dynamic Current Reference Determination of Electrically Excited Synchronous Machines Based on Torque Gradients of Copper Losses. *IEEE Trans. Power Electron.* **2024**, *39*, 7423–7433. [CrossRef]
8. Tang, J.; Liu, Y. Comparison of copper loss minimization and field current minimization for Electrically Excited Synchronous Motor in mild hybrid drives. In *2017 19th European Conference on Power Electronics and Applications (EPE'17 ECCE Europe)*; IEEE: New York, NY, USA, 2017; pp. P.1–P.10. [CrossRef]
9. Goehner, S.; Stoss, J.; Brodatzki, M.; Bachowsky, B.; Liske, A.; Kolb, J.; Hiller, M. New Current Control Strategy for EESMs Based on the Magnetic Equivalent Circuit with Dynamic Decoupling of the d- and e-Axis. In *2023 IEEE 8th Southern Power Electronics Conference and 17th Brazilian Power Electronics Conference (SPEC/COBEP)*; IEEE: New York, NY, USA, 2023; pp. 1–8. [CrossRef]
10. Lee, J.S.; Choi, G. Modeling and hardware-in-the-loop system realization of electric machine drives—A review. *CES Trans. Electr. Mach. Syst.* **2021**, *5*, 194–201. [CrossRef]
11. Mojlish, S.; Erdogan, N.; Levine, D.; Davoudi, A. Review of Hardware Platforms for Real-Time Simulation of Electric Machines. *IEEE Trans. Transp. Electrif.* **2017**, *3*, 130–146. [CrossRef]
12. Tavana, N.R.; Dinavahi, V. Real-Time FPGA-Based Analytical Space Harmonic Model of Permanent Magnet Machines for Hardware-in-the-Loop Simulation. *IEEE Trans. Magn.* **2015**, *51*, 1–9. [CrossRef]
13. Dufour, C.; Lapointe, V.; Belanger, J.; Abourida, S. Hardware-in-the-loop closed-loop experiments with an FPGA-based permanent magnet synchronous motor drive system and a rapidly prototyped controller. In *2008 IEEE International Symposium on Industrial Electronics*; IEEE: New York, NY, USA, 2008; pp. 2152–2158. [CrossRef]
14. Scheer, R.; Bergheim, Y.; Heintges, D.; Rahner, N.; Gries, R.; Andert, J. An FPGA-Based Real-Time Spatial Harmonics Model of a PMSM Considering Iron Losses and the Thermal Impact. *IEEE Trans. Transp. Electrif.* **2022**, *8*, 1289–1301. [CrossRef]
15. Asghari, B.; Dinavahi, V. Experimental validation of a geometrical nonlinear permeance network based real-time induction machine model. In *2012 IEEE Power and Energy Society General Meeting*; IEEE: New York, NY, USA, 2012; pp. 1–15. [CrossRef]
16. Tavana, N.R.; Dinavahi, V. Real-Time Nonlinear Magnetic Equivalent Circuit Model of Induction Machine on FPGA for Hardware-in-the-Loop Simulation. *IEEE Trans. Energy Convers.* **2016**, *31*, 520–530. [CrossRef]
17. Dimitrovski, R.; Luther, M. Model of an Induction Machine with Slot Harmonics for Real-Time Simulation. In *2018 Power Systems Computation Conference (PSCC)*; IEEE: New York, NY, USA, 2018; pp. 1–7. [CrossRef]
18. Zaghrini, C.; Khoury, G.; Fadel, M.; Ghosn, R.; Khatounian, F. Minimum Copper Losses Per Torque Optimization on Electrically Excited Synchronous Motors for Electric Vehicles Applications. In *2022 IEEE 20th International Power Electronics and Motion Control Conference (PEMC)*; IEEE: New York, NY, USA, 2022; pp. 661–666. [CrossRef]
19. Sharaf, A.; Henke, M. Systematic Approach to Design, Modeling and Characterization of Externally Excited Synchronous Machines for Traction Applications. In *2024 IEEE International Conference on Electrical Systems for Aircraft, Railway, Ship Propulsion and Road Vehicles & International Transportation Electrification Conference (ESARS-ITEC)*; IEEE: New York, NY, USA, 2024; pp. 1–6. [CrossRef]
20. Steyaert, B.W.; Swint, E.; Pennington, W.W.; Preindl, M. Piecewise Affine Modeling of Wound-Rotor Synchronous Machines for Real-Time Motor Control. *IEEE Trans. Ind. Electron.* **2023**, *70*, 5571–5580. [CrossRef]
21. Stoß, J.; Geier, L.; Karayel, A.; Decker, S.; Liske, A.; Hiller, M. Unified predictive flux control for EESM, IM, PMSM and SyRM. In *2023 IEEE Energy Conversion Congress and Exposition (ECCE)*; IEEE: New York, NY, USA, 2023; pp. 5009–5019. [CrossRef]
22. Pang, Y.; Knežević, J.M.; Glose, D.; Hackl, C.M. Sensorless Control of Electrically Excited Synchronous Machines Considering Magnetic Saturation and Flux Linkage Dynamics for Automotive Applications. *IEEE Trans. Ind. Electron.* **2024**, *71*, 104–114. [CrossRef]
23. Kurramsetty, V.K.; Balamurali, A.; Korta, P.; Varaha Iyer, K.L.; Kar, N.C. Influence of WFSM Parameters, Currents and Control Scheme on Its Dynamic Performance During Active Short Circuit Fault in EV. In *2021 24th International Conference on Electrical Machines and Systems (ICEMS)*; IEEE: New York, NY, USA, 2021; pp. 564–569. [CrossRef]
24. Kim, Y.; Nam, K. Copper-Loss-Minimizing Field Current Control Scheme for Wound Synchronous Machines. *IEEE Trans. Power Electron.* **2017**, *32*, 1335–1345. [CrossRef]
25. Reinhard, J.; Lohe, K.; Graichen, K. Optimal current setpoint computation for externally excited synchronous machines. In *2022 IEEE Conference on Control Technology and Applications (CCTA)*; IEEE: New York, NY, USA, 2022; pp. 1319–1326. [CrossRef]
26. Hung, K.Y.; Liu, N.W.; Yang, S.C. A Method for Constructing Synchronous Electrical Machine Equivalent Circuit Models for Motor-Drive Co-Simulation. *IEEE Trans. Ind. Appl.* **2025**, *61*, 3114–3130. [CrossRef]

27. Chang, L.; Peng, P. Modeling and Analysis of PWM-Induced Current Ripple in Wound-Field Synchronous Machine. In *2025 IEEE International Electric Machines & Drives Conference (IEMDC)*; IEEE: New York, NY, USA, 2025; pp. 814–819. [CrossRef]
28. Abbas, A.A.; Vesa, J.; Khan, H.; Chen, H.; Liu, Y.; Rasilo, P. Fast and Accurate Non-Linear Model for Synchronous Machines Including Core Losses. *IEEE Trans. Energy Convers.* **2024**, *39*, 2559–2567. [CrossRef]
29. Geng, S.; Prochotta, F.; Aust, M. Generic Modeling Approach for FPGA-Based Real-Time Simulations of Electric Machines. In *2023 IEEE Vehicle Power and Propulsion Conference (VPPC)*; IEEE: New York, NY, USA, 2023; pp. 1–6. [CrossRef]
30. Bontemps, P.; Biner, D.; Münch-Alligné, C.; Dujic, D. Online Loss Calculation and Optimization of an M3C-Driven Externally Excited SM. *IEEE Trans. Ind. Electron.* **2024**, *71*, 5608–5617. [CrossRef]
31. Steinmetz, C.P. *Theorey and Calculation of Alternating Current Phenomena*, 1st ed.; The W. J. Johnston Company: New York, NY, USA, 1897.
32. Richter, J.; Dollinger, A.; Doppelbauer, M. Iron loss and parameter measurement of permanent magnet synchronous machines. In *2014 International Conference on Electrical Machines (ICEM)*; IEEE: New York, NY, USA, 2014; pp. 1635–1641. [CrossRef]
33. Mörée, G.; Leijon, M. Iron loss models: A review of simplified models of magnetization losses in electrical machines. *J. Magn. Magn. Mater.* **2024**, *609*, 172163. [CrossRef]
34. JSOL Corporation. *JMAG Version 23.1—User's Manual: Iron Loss Formulas*; JSOL Corporation: Tokyo, Japan, 2024.
35. Jordan, H. Die ferromagnetischen Konstanten für schwache Wechselfelder. *Elektr. Nachrichtentechnik* **1924**, *1*, 7–29.
36. Hall, G. (Ed.) *Modern Numerical Methods for Ordinary Differential Equations*; Clarendon Press: Oxford, UK, 1976.
37. Richter, J. Modellbildung, Parameteridentifikation und Regelung Hoch Ausgenutzter Synchronmaschinen. Ph.D. Dissertation, Karlsruher Institut für Technologie, Karlsruhe, Germany, 2016. [CrossRef]
38. Ali Matar Bayoumi, M.M. An FPGA-Based Real-Time Simulator for the Analysis of Electromagnetic Transients in Electrical Power Systems. Ph.D. Dissertation, University of Toronto, Toronto, ON, Canada, 2009.
39. Dommel, H. Digital Computer Solution of Electromagnetic Transients in Single-and Multiphase Networks. *IEEE Trans. Power Appar. Syst.* **1969**, *PAS-88*, 388–399. [CrossRef]
40. Rodríguez, B.; González, F.; Naya, M.Á.; Cuadrado, J. Assessment of Methods for the Real-Time Simulation of Electronic and Thermal Circuits. *Energies* **2020**, *13*, 1354. [CrossRef]
41. Geier, L.; Stoß, J.; Liske, A.; Hiller, M. Generalized Inversion of n-dimensional Flux Maps for Unified Nonlinear Machine Models and Predictive Control Algorithms. In *2023 IEEE Energy Conversion Congress and Exposition (ECCE)*; IEEE: New York, NY, USA, 2023; pp. 4821–4828. [CrossRef]
42. Chen, X.; Hu, J.; Chen, K.; Peng, Z. Modeling of electromagnetic torque considering saturation and magnetic field harmonics in permanent magnet synchronous motor for HEV. *Simul. Model. Pract. Theory* **2016**, *66*, 212–225. [CrossRef]
43. dSPACE GmbH. *Solutions & Products: Portfolio & Technologies*; dSPACE GmbH: Paderborn, Germany, 2025.
44. Dufour, C.; Bélanger, J.; Abourida, S. Using Real-Time Simulation in Hybrid Electric Drive and Power Electronics Development: Process, Problems and Solutions. In *Proceedings of the SAE Technical Paper Series*; SAE Technical Paper Series; SAE International400 Commonwealth Drive: Warrendale, PA, USA, 2006. [CrossRef]
45. Schulte, T.; Kiffe, A.; Puschmann, F. HIL Simulation of Power Electronics and Electric Drives for Automotive Applications. *Electron. ETF* **2012**, *16*, 2. [CrossRef]